

Alfvén wave heating of heavy ions in the expanding solar wind: Hybrid simulations

Petr Hellinger,¹ Marco Velli,^{2,4} Pavel Trávníček,¹ S. Peter Gary,³ Bruce E. Goldstein,⁴ and Paulett C. Liewer⁴

Abstract. We present hybrid expanding box simulations of the interaction of left-handed Alfvén waves with protons, alpha particles and a tenuous population of oxygen O⁵⁺. The Alfvén waves are initially nonresonant with the ions and the expansion bring them to the cyclotron resonance with O⁵⁺ ions, then with alpha particles, and finally with protons. The simulations show that O⁵⁺ ions are efficiently heated in the directions perpendicular to the background magnetic field, but are only slightly accelerated. Oxygen scattering has a finite time span and saturates mainly due to the marginal stabilization with respect to the oxygen cyclotron instability generated by the temperature anisotropy. During the scattering oxygen ions are able to absorb only a limited amount of available fluctuating energy and, for the parameters used in the simulations, their presence has a minimum influence on alpha particles and protons.

1. Introduction

Solar coronal heating still presents many unsolved mysteries, which, for the open solar corona, are confounded by the rapid transition from a collisional to a collisionless plasma. SOHO spacecraft observations of strong temperature anisotropies of minor ions [Kohl *et al.*, 1998; Li *et al.*, 1998] indicate heating perpendicular to the background magnetic field. A natural source of such heating is the cyclotron resonance with Alfvén left-handed waves, as described in the reviews by Tu and Marsch [1995] and Hollweg and Isenberg [2002].

One possible source of cyclotron resonances of the ions with the waves is the frequency sweeping mechanism [e.g. Tu and Marsch, 2001, and references therein]: As low-frequency, left-handed Alfvén waves propagate upward in the coronal holes the ambient magnetic field decreases (as does the ion cyclotron frequency) so that the waves eventually become resonant with minor ions with the lowest gyrofrequency. These ions are heated and accelerated by the (quasi-linear) resonant interaction. It is expected that the amount of energy absorbed by minor ions which are low in abundance is small and that the heating and acceleration saturate. The ions with the second lowest gyrofrequency are in turn heated and accelerated, and so forth. The key question of this scenario is the saturation mechanism which determines the amount of available energy for each ion species, most importantly for alpha particles and protons.

The cyclotron wave-particle interaction in the context of the corona and the solar wind has been studied using a wide range of models with varied approximations [Hollweg and Isenberg, 2002]. These models give often very different predictions so that their results indicate a need of a self-consistent approach [Tu and Marsch, 2001]. Models of this wave-particle interaction includes linear Vlasov analysis, quasi-linear models and direct kinetic simulations.

Linear analyses give information about wave dispersion and damping properties. The cold plasma approximation shows that for strictly parallel propagation there exists a left-handed branch

for each ion species with gaps around each ion cyclotron frequency. Such a gap would impede wave energy transfer to the next higher ion cyclotron resonance. The more physical, linear Vlasov theory in a Maxwellian plasma [Isenberg, 1984] shows that these gaps are not always present; they disappear for sufficiently hot or sufficiently tenuous ions. Furthermore, a non-zero differential velocity of a resonant ion species with respect to another ion species may remove the gap so that fluctuation energy may go to the next highest ion cyclotron frequency [Gomberoff *et al.*, 1996]. An extension of the linear analysis to bi-Maxwellian distributions indicate that ion temperature anisotropies do not change the frequency dispersion, but rather change the damping/growth rate [cf. Ofman *et al.*, 2001; Gary *et al.*, 2001a]. In general, the dispersion/damping of the cyclotron waves strongly depends on the resonant portion of the distribution function; the cyclotron resonant condition of a left-handed, parallel propagating wave with k and ω (assuming $k > 0$ and $\omega > 0$) with ion species s reads

$$kv_{\parallel} = \omega - \omega_{cs} \quad (1)$$

(for symbol definitions see Appendix).

Quasi-linear models [Galinsky and Shevchenko, 2000; Cranmer, 2001; Vocks and Marsch, 2002] stress the fact that diffusion resulting from the cyclotron resonance generates non-Maxwellian distribution functions. Cyclotron diffusion leads to a formation of a quasi-linear plateau in the resonant region of the velocity distribution functions upon which cyclotron waves become marginally stable. This plateau resulting from the interaction with a spectrum of non-dispersive left-hand polarized, parallel propagating waves consists of surfaces, shells centered around the wave phase velocity:

$$\left(v_{\parallel} - \frac{\omega}{k}\right)^2 + v_{\perp}^2 = \text{const.} \quad (2)$$

In a case of dispersive waves the plateau becomes more complicated [Isenberg and Lee, 1996]. In situ solar wind observations [Marsch and Tu, 2001] indicate existence of such plateaux in proton distribution functions.

The quasi-linear models by Cranmer [2001] and Vocks and Marsch [2002] showed that the minor ions are strongly energized by the cyclotron waves. The energization saturates near marginal stability and the remaining wave energy is available for the higher gyrofrequency ions. The two models also indicate that low-abundance ion species may absorb most if not all of the fluctuating energy. Cranmer [2001] suggest that other mechanisms are to be invoked to account for observations [e.g. of O⁵⁺, cf. Kohl

¹Institute of Atmospheric Physics, AS CR, Prague, Czech Republic

²Department of Astrophysics and Space Science, University of Florence, Italy

³Los Alamos National Laboratory, Los Alamos, New Mexico, USA

⁴Jet Propulsion Laboratory, Pasadena, California, USA

et al., 1998]. However, the models of [Cranmer, 2001; Vocks and Marsch, 2002] are limited by the fact that they neglect the influence of minor ions on the dispersion relation.

To date there are few kinetic numerical simulations of the cyclotron interaction. *Ofman et al.* [2002] and *Xie et al.* [2004] used a hybrid code where the wave energy was continuously injected into the simulated system. On the other hand, *Liewer et al.* [2001] used a hybrid expanding box model which in an idealized way includes solar wind expansion and the frequency sweeping effect. All these numerical studies indicate that the cyclotron interaction is not efficient for ion acceleration and show rather strong energization of minor ions in the perpendicular direction in agreement with the character of the cyclotron resonance (equation (2)) and with the results of the quasi-linear models. The numerical studies suggest that saturation is not due to the dispersion change owing to an increase of the ion/ion differential velocity [Gomberoff *et al.*, 1996].

In this paper we investigate the frequency sweeping mechanism using the hybrid expanding box model [Liewer *et al.*, 2001]. We consider a plasma consisting of electrons, protons, alpha particles and a tenuous population of O^{5+} . The system is initialized with a flat spectrum (i.e. with a zero spectral index) of low-amplitude, low-frequency left-handed Alfvén waves. The initial waves are relatively far from the resonance with ions and as the system expands the waves become resonant with ions, O^{5+} being the first resonant species. We investigate the evolution of the expanding system and concentrate on the heating and acceleration of the O^{5+} ions and the corresponding saturation mechanism.

The paper is organized as follows: First, we describe the simulation method and its theoretical properties (section 2). Then, in section 3, we study the evolution of the expanding plasma and the frequency sweeping mechanism in a case of a transverse expansion (subsection 3.1) and in a case of a combination of the transverse and radial expansion (subsection 3.2). In subsection 3.3 we investigate the property of the saturation using a set of simulations with different initial conditions and expansion types. Finally, in section 4 we discuss the simulation results within the context of observations and theoretical models of the evolution of MHD turbulence in the outer corona and accelerating solar wind. In Appendix we give symbol definitions.

2. Hybrid expanding box model

In this paper we use a modified version of a 1-D hybrid code [Matthews, 1994; Hellinger *et al.*, 2003a, b], a Hybrid Expanding Box (HEB) code. The HEB code captures some of the effects of the global solar wind structure on the local plasma. The fast solar wind propagates from the sun and its velocity \mathbf{U} has roughly *tanh* dependence on the distance from the sun $R = |\mathbf{R}|$ and is roughly radial, $\mathbf{U} = \mathbf{U}\mathbf{R}/R$ where $U = |\mathbf{U}|$. At a given distance R the radial flow with the velocity U translates locally as an expansion: If we consider a small volume of plasma, its transverse and radial sizes l_{\perp} and l_{\parallel} expand as

$$\frac{dl_{\perp}}{dt} = \frac{U}{R}l_{\perp} \quad \text{and} \quad \frac{dl_{\parallel}}{dt} = \frac{dU}{dR}l_{\parallel}, \quad (3)$$

respectively. The transverse and radial expansion is characterized by

$$t_{\perp} = \frac{R}{U} \quad \text{and} \quad t_{\parallel} = \left(\frac{dU}{dR}\right)^{-1}, \quad (4)$$

the transverse and radial expansion time, respectively. Figure 1 shows the solar wind velocity U (in km/s), the transverse and radial characteristic expansion times t_{\perp} and t_{\parallel} (in units of the inverse local proton cyclotron frequency ω_{cp}) as functions of the radial distance R from the sun (in units of the solar radius R_{\odot}) in a model solar wind [cf. *Casalbuoni et al.*, 1999]. This is a fluid model with proton and electron temperatures empirically determined to fit observations at 1 AU and close to the sun, including magnetic field strength, density, turbulence amplitudes, temperatures and their measured gradients.

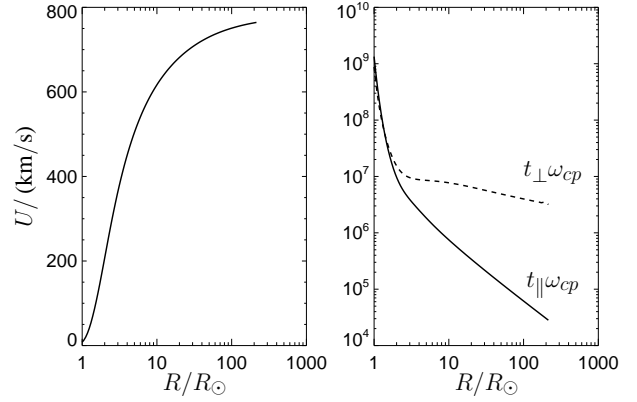


Figure 1. Model solar wind [Casalbuoni *et al.*, 1999]: (left) The solar wind velocity U as a function of the radial distance R . (right) Transverse and radial characteristic expansion times t_{\perp} and t_{\parallel} (in units of the inverse local proton cyclotron frequency ω_{cp}) as functions of R . R is given in units of R_{\odot}

Figure 1 shows that solar wind expansion times to and beyond 1 AU are much greater than the local proton gyroperiod. In the corona the two expansion times t_{\perp} and t_{\parallel} are comparable, but further from the sun the transverse expansion dominates.

In HEB computer models expansion is induced by an external force that drive the physical lengths \mathbf{x} to evolve $\mathbf{x} = \mathbf{L} \cdot \xi$ where \mathbf{L} is a diagonal matrix $\mathbf{L} = \text{diag}(L_{\parallel}, L_{\perp}, L_{\perp})$ with

$$L_{\perp}(t) = 1 + t/t_{\perp} \quad \text{and} \quad L_{\parallel}(t) = 1 + t/t_{\parallel} \quad (5)$$

following equation (3). The code solves the evolution of the system in the coordinates ξ and $\nu = d\xi/dt$ co-moving with the expansion, see *Hellinger and Trávníček* [2005] for a detailed description of the general governing equations.

Units of space and time are the initial proton inertial length c/ω_{pp0} and the inverse initial proton cyclotron frequency $1/\omega_{cp0}$, respectively (for symbol definitions see Appendix). Fields and moments are defined on a 1-D grid with $N_x = 2048$ grid points with the spatial resolution is $\Delta x = c/\omega_{pp0}$ so that the box size is $L_x = 2048c/\omega_{pp0}$. The code uses the periodic boundary conditions and there are 1024 particles per cell for protons, 512 for alpha particles, and 128 for other ion species. The time step for the particle advance is $\Delta t = 0.025/\omega_{cp0}$, while the magnetic field \mathbf{B} is advanced with a smaller time step $\Delta t_B = \Delta t/4$. The initial background magnetic field is $\mathbf{B}_0 = (B_0, 0, 0)$.

During the simulation the plasma expands and the plasma properties vary with time; the density decreases as

$$n \propto L_{\perp}^{-2} L_{\parallel}^{-1}. \quad (6)$$

Flux conservation in the expanding box implies that the radial component B_{\parallel} of the magnetic field decreases as

$$B_{\parallel} \propto L_{\perp}^{-2}, \quad (7)$$

whereas the transverse components should decrease as

$$B_{y,z} \propto L_{\perp}^{-1} L_{\parallel}^{-1} \quad (8)$$

but, because transverse magnetic field fluctuations are coupled to velocity fluctuations in Alfvén waves, one expect transverse magnetic field fluctuations to follow WKB behavior, see below.

If the plasma expansion is slow compared to the ion gyration period and there are no additional kinetic heating or acceleration processes, one expects that the first and second adiabatic invariant are conserved so that, as follows from equations (6) and (7), the ion temperature anisotropy, parallel beta and Alfvén velocity should evolve as

$$\begin{aligned} \frac{T_{s\perp}}{T_{s\parallel}} &\propto \frac{B^3}{n^2} \propto \left(\frac{L_{\parallel}}{L_{\perp}}\right)^2 \\ \beta_{s\parallel} &\propto \frac{n^3}{B^4} \propto \frac{L_{\perp}^2}{L_{\parallel}^3} \\ v_A &\propto \frac{B}{\sqrt{n}} \propto \frac{\sqrt{L_{\parallel}}}{L_{\perp}} \end{aligned} \quad (9)$$

(where we have neglected transverse magnetic field fluctuations and set $B = |B_{\parallel}|$).

An amplitude of fluctuating magnetic field δB for an Alfvén wave with $\omega = kv_A$ in a slowly expanding plasma is expected to follow WKB approximation. The wave action $S = \delta B^2/\omega$ is conserved

$$\int \frac{\delta B^2}{\omega} d^3x = \text{const.} \quad (10)$$

When we take into account that the volume increases as $L_{\perp}^2 L_{\parallel}$, that a parallel wave vector decreases as L_{\parallel}^{-1} and that the Alfvén velocity follows equation (9) we have [cf. *Liewer et al.*, 2001]:

$$\delta B \propto L_{\perp}^{-3/2} L_{\parallel}^{-3/4}. \quad (11)$$

In the following section we present effective perpendicular ion temperatures (equation (A1)) which include a contribution from the Alfvén fluctuating velocities. If we denote δu as the amplitude of the Alfvén fluctuating velocities with $\delta u \propto \delta B$ and assuming CGL and WKB behavior, equations (9) and (11) imply that the contribution of the Alfvén fluctuating velocities to the effective temperature anisotropy scales as

$$\frac{(\delta u)^2}{T_{\parallel}} \propto L_{\parallel}^{1/2} L_{\perp}^{-3}. \quad (12)$$

This implies that the late-time contribution of the fluctuating velocities should be small in our simulations.

3. Simulation results

We now investigate the interaction of Alfvén waves in a multi-ion plasma, using HEB simulations of wave-particle interactions including protons, alpha particles and a small abundance of oxygen O^{5+} . Following *Liewer et al.* [2001] we initialize all the simulations with a flat spectrum of parallel propagating, left-handed, circularly polarized waves: Initially, there are $n_k = 50$ modes of wave vectors k ranging from $k_{\min} = 2\pi/L_x \approx 0.003c/\omega_{pp0}$ (the minimum wave vector in the periodic box with the size L_x) to $k_{\max} = 100\pi/L_x \approx 0.153c/\omega_{pp0}$, with $\delta \mathbf{B}_k \perp \mathbf{B}_0$. These modes have random phases ϕ_k and the same amplitudes $|\delta \mathbf{B}_k|/B_0 = 5 \times 10^{-3}$,

$$\delta \mathbf{B} = \sum_k \delta \mathbf{B}_k e^{i(kx - \omega_k t + \phi_k)} \quad (13)$$

where k and ω_k are related through the cold-plasma dispersion relation

$$\omega_k^2 \sum_s \frac{m_s n_s}{1 - \frac{\omega_k}{\omega_{cs}}} = \rho v_A^2 k^2. \quad (14)$$

The initial wave beta is $\beta_w = 1.25 \times 10^{-3}$. The cold-plasma dispersion relation, equation (14), has many different solutions. We choose the solution with the lowest-frequency (oxygen) branch corresponding to MHD Alfvén waves.

The ion distribution functions f_s are initialized as

$$f_s = f_s(x, t, \mathbf{v}) = \frac{n_s}{\pi^{3/2} v_{ths}^3} e^{-\frac{(\mathbf{v} - \mathbf{u}_s)^2}{2v_{ths}^2}}. \quad (15)$$

where the mean velocity \mathbf{u}_s of the species s is given by

$$\mathbf{u}_s = - \sum_k \frac{\omega_k}{k} \frac{1}{(1 - \frac{\omega_k}{\omega_{cs}})} \frac{\delta \mathbf{B}_k}{B_0} e^{i(kx - \omega_k t + \phi_k)} \quad (16)$$

Note that the distribution functions (equation (15)) are not a stationary solution of the Vlasov equation owing to the superposition of different wave-vectors (the notion of linearity is different in the MHD and the Vlasov approximations) and even owing to second order thermal terms in \mathbf{v} for each mode. In order to avoid any possible problems with the fact that equation (15) is not an exact stationary solution of the Vlasov equation, we start the simulations with cold ions.

All our simulations consider a plasma with protons, alpha particles and a small abundance of O^{5+} ions. All the species are initially isotropic, and low beta values are used in all runs. Protons have $\beta_{p0} = 10^{-2}$, alpha particles have $n_{\alpha}/n_e = 5 \cdot 10^{-2}$ and $\beta_{\alpha 0} = 5.5 \cdot 10^{-4}$, and oxygen O^{5+} ions have $n_{O}/n_e = 10^{-4}$ and $\beta_{O0} = 2.2 \cdot 10^{-6}$. Table 1 provides an overview of the initial parameters for the simulations we study in the next subsections. It is important to note that for the plasma parameters given in Table 1 the Vlasov linear theory predicts a cold plasma-like dispersion (equation (14)).

3.1. Transverse Expansion

First we investigate a plasma in a slow expansion with the transverse expansion time $t_{\perp} = 2000$ and no radial expansion, $L_{\parallel} = 1$ in run 1. During the expansion the frequencies of the Alfvén waves increase with respect to the ion cyclotron frequencies. It is the oxygen O^{5+} which first becomes resonant with the waves: O^{5+} ions are heated and accelerated via the cyclotron resonance. Later, after the oxygen heating is saturated, the alpha particles are heated, and, finally, also protons are heated.

For run 1, Figure 2 (left) displays the parallel temperature $T_{\parallel s}$ and (right) the effective temperature anisotropy $T_{\perp s}/T_{\parallel s}$ as functions of time for the three species: (solid) protons, (dashed) alpha particles, and (dash-dotted) O^{5+} . Solid circles denote the time of the oxygen maximum temperature anisotropy. Note that the Alfvén fluctuating velocities contribute to the effective perpendicular temperatures, see equations (12) and (A1). The ion parallel temperature follows quite closely the CGL predictions (i.e. have almost constant values); only in case of O^{5+} there is a clear sign of the parallel cooling before the saturation time (Figure 2, left panel, solid circle) and a parallel heating just after this point. The interaction between the ions and the spectrum of Alfvén waves results in a perpendicular heating. The heating induces a strong temperature anisotropy for O^{5+} at $t \sim 2t_{\perp}$ and slows the adiabatic perpendicular cooling of the alpha particles at $t \sim 3t_{\perp}$ and the protons at $t \sim 6t_{\perp}$ (Figure 2, right panel). The duration of heating of oxygen ions and alpha particles has a time span of a few t_{\perp} . After this time the heating saturates. The oxygen parallel heating after the saturation may be a consequence of the oxygen cyclotron instability driven by the strong temperature anisotropy.

Table 1. Initial parameters of the HEB simulations

Run	n_O/n_e	β_O	$t_{\perp}\omega_{cp0}$	$t_{\parallel}\omega_{cp0}$
1	2×10^{-4}	2.2×10^{-6}	2×10^3	
1b			2×10^3	
2	2×10^{-4}	2.2×10^{-6}	2×10^3	4×10^3
2b			2×10^3	4×10^3
3	2×10^{-4}	2.2×10^{-7}	2×10^3	
4	2×10^{-4}	2.2×10^{-5}	2×10^3	
5	2×10^{-4}	2.2×10^{-4}	2×10^3	
6	2×10^{-4}	2.2×10^{-5}	2×10^3	4×10^3
7	2×10^{-4}	2.2×10^{-6}	2×10^3	8×10^3
8	2×10^{-4}	2.2×10^{-5}	2×10^3	8×10^3
$\beta_p = 10^{-2}, n_{\alpha}/n_e = 5 \times 10^{-2}, \beta_{\alpha} = 5.5 \times 10^{-4}$ $\beta_w = 1.25 \times 10^{-3}, \delta \mathbf{B}_k /B_0 = 5 \times 10^{-3} k^0$				

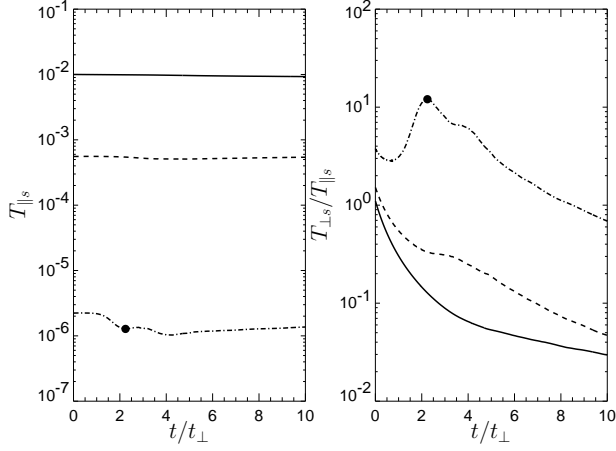


Figure 2. Time evolution in run 1: (left) the parallel temperature $T_{\parallel s}$ (in arbitrary units) and (right) the effective temperature anisotropy $T_{\perp s}/T_{\parallel s}$ as functions of time for the three species: (solid) protons, (dashed) alpha particles, and (dash-dotted) O^{5+} . Solid circles denote the time of the oxygen maximum temperature anisotropy.

The expanding box model replaces the spatial dependence of the solar wind with the temporal one; the time dependence of Figure 2 gives essentially the radial dependence as $R \propto 1 + t/t_{\perp}$. The time (as well as the radial distance) is also related to the plasma parameters as $\beta_{\parallel s}$ and $T_{\perp s}/T_{\parallel s}$; this relation is simply the CGL equation (9) when no wave-particle interaction is present but is more complex otherwise as shown in Figure 3: The left panel of Figure 3 shows the system evolution as a path in the space $(\beta_{\parallel s}, T_{\perp s}/T_{\parallel s})$ for the three species: (solid) protons, (dashed) alpha particles, and (dash-dotted) O^{5+} . Solid circles denote the time of the oxygen maximum temperature anisotropy whereas the dotted curves denote the prediction of CGL theory. This panel clearly demonstrates the departure of the ion behavior from CGL theory which appears first for O^{5+} , then for the alpha particles and, finally, for the protons.

In order to compare simulation results with the linear theory we have investigated the growth rate γ of the oxygen cyclotron instability in a homogeneous plasma which consists of isotropic Maxwellian electrons, protons and alpha particles and of anisotropic bi-Maxwellian oxygen O^{5+} ions. Namely, we have calculated the dispersion $\omega = \omega(k)$ for wave vectors in the interval $0.01 \leq k \leq 2.5$ for a set of oxygen parameters: $10^{-7} \leq \beta_{\parallel O} \leq 10$ and $1 \leq T_{\perp O}/T_{\parallel O} \leq 100$. The temperatures of alpha particles and protons are assumed to be mass-proportional, $T_s = m_s T_{\parallel O}/m_O$ and the electron beta is $\beta_e = 0.1$. For each $\beta_{\parallel O}$ and $T_{\perp O}/T_{\parallel O}$ (and the corresponding temperatures of protons and alpha particles) we have calculated the maximum growth rate γ in the interval $0.001 \leq k \leq 1.5$. The result of this calculation, $\gamma = \gamma(\beta_{\parallel O}, T_{\perp O}/T_{\parallel O})$ is shown in Figure 3 as a gray-scale plot: Darker gray denotes stronger instability whereas white corresponds to stable or marginally stable region. The boundary between the white and gray regions of Figure 3 corresponds to the value of the maximum growth rate $\gamma = 10^{-4} \omega_{cp}$ and may be approximately given in a form [Ofman et al., 2001; Gary et al., 2001b]

$$T_{\perp O}/T_{\parallel O} - 1 \sim 0.7(\beta_{\parallel O} \frac{n_e m_p}{n_O m_O})^{-0.4}. \quad (17)$$

The right panel of Figure 3 shows the evolution of run 1 in the space $(\beta_{\parallel s}, v_{\parallel s}/v_A)$ for the three species: (solid) protons, (dashed) alpha particles, and (dash-dotted) O^{5+} ; $v_{\parallel s}$ is the mean parallel ion velocity and v_A is the local Alfvén velocity, Figure 3 (right panel) shows that the wave-particle interactions also give rise to a differential velocity between different ion species, as was previously shown by [Liewer et al., 2001]. The O^{5+} ions are only slightly accelerated (with respect to protons); the oxygen/proton velocity remains a small fraction of the local Alfvén velocity. Note that after alpha-particle saturation the alpha particles are decelerated to negative

velocities with respect to protons. There is no discernible acceleration of protons. For oxygen ions $v_{\parallel O}/v_A$ increases even after the saturation; this may partly be a result of the oxygen cyclotron instability but mainly it is a consequence of the fact, that the local Alfvén velocity v_A decreases with time, as in equation (9).

A noteworthy simulation feature is the oxygen heating saturation in the region where the bi-Maxwellian linear theory predicts growth of the O^{5+} cyclotron instability; the saturation lies close to the theoretical marginal threshold of this instability. Figure 3 indicates that the O^{5+} cyclotron instability is active and may explain the parallel oxygen heating (see Figure 2, left panel), however, the comparison between the linear theory and the simulations is at most semi-quantitative: First, the linear theory is calculated for bi-Maxwellian oxygen ions whereas the actual oxygen distribution function is relatively far from a bi-Maxwellian shape (see below). Second, the perpendicular temperatures include contributions from the Alfvén fluctuating velocities; however equation (12) predicts that the contribution of the Alfvén fluctuating velocities rapidly decreases as the system expands.

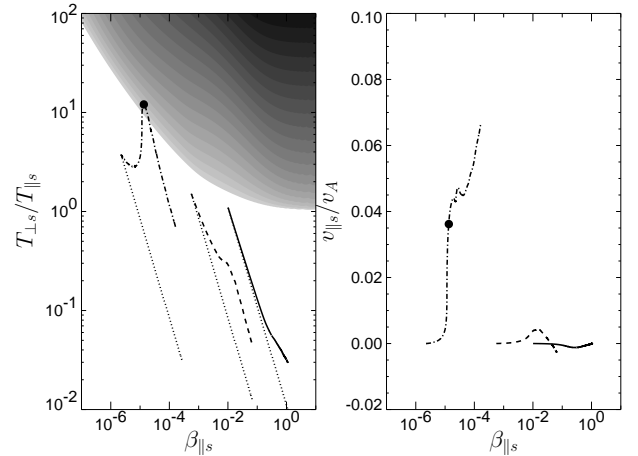


Figure 3. Evolution in run 1: (left) The system path in the space $(\beta_{\parallel s}, T_{\perp s}/T_{\parallel s})$ for the three species: (solid) protons, (dashed) alpha particles, and (dash-dotted) O^{5+} . The dotted curves denote the corresponding predictions of CGL theory and the gray-scale plot denotes the region unstable with respect to the O^{5+} cyclotron instability (in bi-Maxwellian plasma). (right) The system path in the space $(\beta_{\parallel s}, v_{\parallel s}/v_A)$ for the three species: (solid) protons, (dashed) alpha particles, and (dash-dotted) O^{5+} . Solid circles denote the time of the oxygen maximum temperature anisotropy.

The heating and acceleration of different ion species is done at the expense of the Alfvén wave energy. It is interesting to investigate the amount of wave energy absorbed by the different species. The fluctuating wave energy δB is expected to follow the WKB predictions of equation (11) when far from the ion cyclotron resonances. The evolution of the wave energy is shown in Figure 4. The left panel of Figure 4 shows the gray scale plot of the fluctuating magnetic field δB multiplied by the WKB factor $(1 + t/t_{\perp})^{3/2}$ as a function of wave vector k and time t . The overplotted curve show the approximate cyclotron resonance condition $k v_A = \omega_{cs}$ (see equation (1)) for (solid) protons, (dashed) alpha particles, and (dash-dotted) O^{5+} .

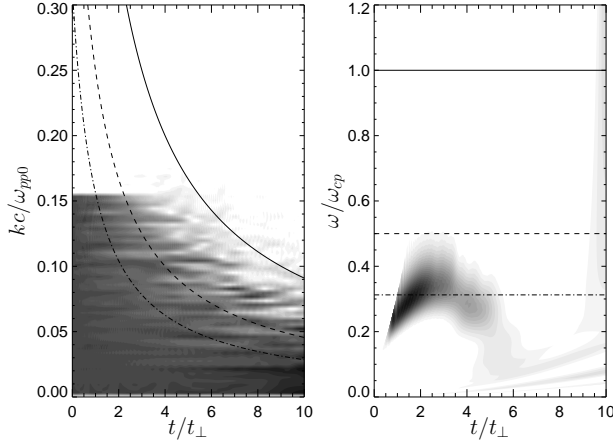


Figure 4. Time evolution in run 1: (left) The gray scale plot of the fluctuating magnetic field δB multiplied by the factor $(1 + t/t_\perp)^{3/2}$ as a function of time t and of wave vector k . The overplotted curves show the approximate cyclotron resonance condition $kv_A = \omega_{cs}$ for (solid) protons, (dashed) alpha particles, and (dash-dotted) O^{5+} . (right) The gray scale plot of the fluctuating magnetic field $\delta B_{k_{\max}}$ multiplied by the WKB factor $(1 + t/t_\perp)^{3/2}$ as a function of time t and frequency ω normalized to ω_{cp} . The overplotted lines show the ratio ω_{cs}/ω_{cp} for (solid) protons, (dashed) alpha particles, and (dash-dotted) O^{5+} .

The right panel of Figure 4 shows the gray scale plot of the fluctuating magnetic field $\delta B_{k_{\max}}$ for the wave vector k_{\max} as a function of time t and frequency ω (normalized to ω_{cp}). The spectrum $\delta B_{k_{\max}}(t, \omega)$ was calculated using the Morlet wavelet transform [Torrence and Compo, 1998] of $\delta B_{k_{\max}}(t)$. The overplotted lines show the cyclotron frequency ω_{cs}/ω_{cp} for (solid) protons, (dashed) alpha particles, and (dash-dotted) O^{5+} .

Figure 4 (left panel) shows that the wave amplitude δB_k for the different wave vectors k indeed follows the WKB prediction of equation 11

$$\delta B \left(1 + \frac{t}{t_\perp}\right)^{3/2} \sim \text{const} \quad (18)$$

when far from the ion cyclotron resonances. The level of fluctuation only slightly changes when passing through the oxygen resonance whereas the passage through the alpha resonance damps significantly the wave amplitude. Figure 4, right panel, confirms this result: the evolution of the frequency for $\delta B_{k_{\max}}$ does show not any significant change near the cyclotron resonance of O^{5+} . Figure 4 indicates that the amount of energy absorbed by oxygen is small with respect to the available wave energy. Figure 4 also clearly shows no cold plasma-like frequency gap at the O^{5+} cyclotron frequency ω_{cO} but indicates a presence of such a gap near the alpha cyclotron frequency $\omega_{c\alpha}$. The frequency spectrum remains below the alpha cyclotron frequency which seems to block the energy from passing closer to the proton cyclotron frequency ω_{cp} where the resonance with protons is more efficient – the sweeping mechanism is blocked. Note that due to the finite-time data interval used for the wavelet transform the wave spectrum (Figure 4, right panel) has some artificial features near the two boundaries: the cut-off near $t = t_\perp$, the two or three lines for $\omega \sim 0.2\omega_{cp}$ at $t > 6t_\perp$, and the amplitude enhancement near $t = 10t_\perp$ for $\omega > 0.5\omega_{cp}$.

Figures 2 and 3 indicate presence of oxygen cyclotron instability. On the other hand, Figure 4 shows no discernible increase of the wave amplitude which would correspond to this instability. A natural explanation of this result may be the small abundance of oxygen ions: the tenuous ions are able to emit only a small amount of energy through the cyclotron instability.

If the heating and acceleration of O^{5+} saturates, one expects formation of the quasi-linear plateau (equation (2)). Indeed the veloc-

ity distribution of O^{5+} at maximum temperature anisotropy is far from bi-Maxwellian and is partially shell-like as documented in Figure 5. Figure 5 shows the reduced (i.e., gyrophase averaged) oxygen distribution function $\tilde{f}_O = \tilde{f}_O(v_\parallel, v_\perp)$ (left) at the time of the maximum anisotropy (see Figures 2 and 3, solid circles) and (right) at the end of the simulation. Note that the Alfvén fluctuating velocities contribute to the perpendicular velocities and that $\tilde{f}(v_\parallel, v_\perp)$ has been calculated from equation (A2) with a singular region $v_\perp \sim 0$. The singular region is not consequently well-represented. The reduced distribution function at the time of the temperature anisotropy is relatively complex, probably owing to the combination of the three processes taking place at the same time – transverse expansion, interaction with the initial, probably dispersive, Alfvén wave spectrum and growth of the oxygen cyclotron instability (the contribution of the Alfvén fluctuating velocities at the saturation is not important as may be argued in similar way as in equation (12)). We shall return to this problem in the next section comparing the results of runs 1 and 2. Figure 5 (right panel) shows the oxygen distribution function at the end of the simulation. The distribution function keeps the signature of the cyclotron scattering only for $v_\parallel < 0.02v_A$. The distribution is shrunk in v_\perp and prolonged in v_\parallel as a result of the CGL-like behavior. Figure 5 (right panel) indicates that the particles (with $v_\parallel > 0.02$) are not resonant with the imposed waves.

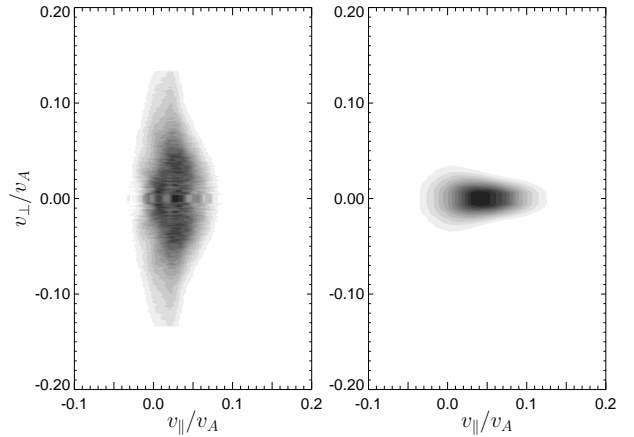


Figure 5. Gray scale plot of the reduced oxygen distribution function $\tilde{f}_O = \tilde{f}_O(v_\parallel, v_\perp)$ (left) at the time of the maximum temperature anisotropy (see Figures 2 and 3, solid circles) and (right) at the end of the simulation.

The results of run 1 indicated that the amount of fluctuating energy absorbed by O^{5+} is small and that the presence of O^{5+} does not influence alpha particles and protons. In order to test this hypothesis we performed run 1b without O^{5+} but with the other parameters identical to the those of run 1 (see Table 1). Run 1b gives essentially the same results for alpha particles and protons as in run 1. On the quantitative level the maximum relative difference in the fluctuating magnetic energies in run 1 and 1b is about 1.5 %; this difference is mainly the amount of energy absorbed by the oxygen O^{5+} (the wave energy emitted via the cyclotron instability is negligible). Comparison of runs 1 and 1b indicate that in the present case the oxygen O^{5+} has a status of test particles and its presence has little or no influence on alpha particles and protons. We have performed an additional set of simulations with small abundances (of the order of 10^{-6}) of O^{5+} , O^{6+} and Mg^{9+} . In these simulations we have observed a similar behavior as in run 1: The presence of these minor ions had little or no influence on alpha particles and protons.

In addition simulations with different combinations of these minor ions no influence on each other was observed.

3.2. Radial Expansion

The outward flow of the solar wind gives rise to both a transverse and a radial expansion of the plasma. Both expansions importantly influence solar wind properties. The main feature of the radial expansion is that it cools parallel temperatures. So we expect temperature anisotropies in the double expansion simulations be significantly different from those in the case of run 1 with no radial expansion.

In run 2 the same initial conditions are used as in run 1; however, we added the radial expansion with the expansion time $t_{\parallel} = 2t_{\perp} = 4000$ (see Table 1). The evolution of the system in run 2 is shown in Figure 6 which displays (left) the parallel temperature $T_{\parallel s}$ and (right) the effective temperature anisotropy $T_{\perp s}/T_{\parallel s}$ as functions of time (in the same format as used in Figure 2) for the three species: (solid) protons, (dashed) alpha particles, and (dash-dotted) O^{5+} . Solid circles denote the oxygen maximum temperature anisotropy point. Figure 6 demonstrate the effect of the radial expansion – the parallel cooling: Figure 6 (left panel) shows that the parallel temperatures of protons and alpha particles follow quite closely CGL predictions whereas oxygen ions are additionally cooled in the parallel direction before saturation and heated afterward. Figure 6 (right panel) shows that oxygen ions are moreover strongly heated in the perpendicular direction whereas protons and alpha particles are only slightly heated. The duration of the oxygen heating has a time span of only a few t_{\perp} . After this time the heating saturates similarly to the case of run 1.

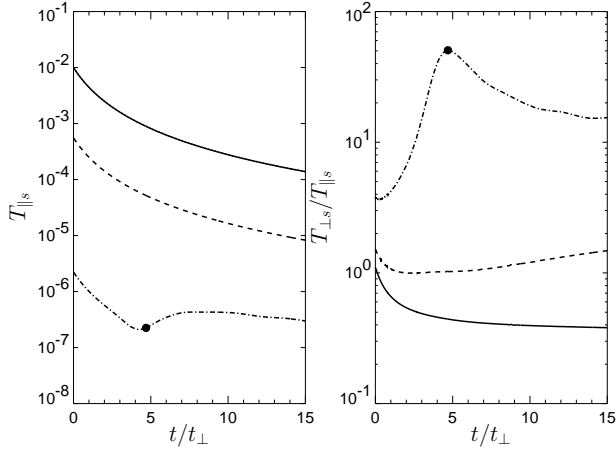


Figure 6. Time evolution in run 2: (left) the parallel temperature $T_{\parallel s}$ (in arbitrary units) and (right) the effective temperature anisotropy $T_{\perp s}/T_{\parallel s}$ as functions of time for the three species: (solid) protons, (dashed) alpha particles, and (dash-dotted) O^{5+} . Solid circles denote the oxygen maximum temperature anisotropy point.

Figure 7 displays the evolution of ion parameters in the same format as used in Figure 3: The left panel of Figure 7 shows the system path in the space $(\beta_{\parallel s}, T_{\perp s}/T_{\parallel s})$ for the three species: (solid) protons, (dashed) alpha particles, and (dash-dotted) O^{5+} . The dotted curves denote the prediction of CGL whereas the gray-scale plot denotes the region unstable with respect to O^{5+} cyclotron instability. The right panel of Figure 7 shows the system path in the space $(\beta_{\parallel s}, v_{\parallel s}/v_A)$ for three species: (solid) protons, (dashed) alpha particles, and (dash-dotted) O^{5+} . Solid circles denote the oxygen maximum temperature anisotropy point.

Figure 7 (left panel) clearly demonstrates the departure of the ion behavior from CGL theory which appear first for O^{5+} , then for the alpha particles and, finally, for the protons. The maximum oxygen temperature anisotropy is higher than in run 1 and lies in the

region unstable with respect to the oxygen cyclotron instability (in bi-Maxwellian plasma). Moreover, the evolution after saturation exhibits features of a marginal stability path [cf. *Hellinger et al.*, 2003b; *Hellinger and Trávníček*, 2005] with respect to the oxygen instability.

Figure 7 (right panel) shows that at the same time oxygen ions are only slightly accelerated (with respect to protons); the oxygen/proton velocity is a small fraction of the local Alfvén velocity. On the other hand, there is no discernible acceleration of the alpha particles and protons. For oxygen ions $v_{\parallel O}/v_A$ increases even after the saturation; this is may partly be a result of the oxygen cyclotron instability but mainly it is a consequence of the fact, that the local Alfvén velocity v_A decreases with time, as in equation (9).

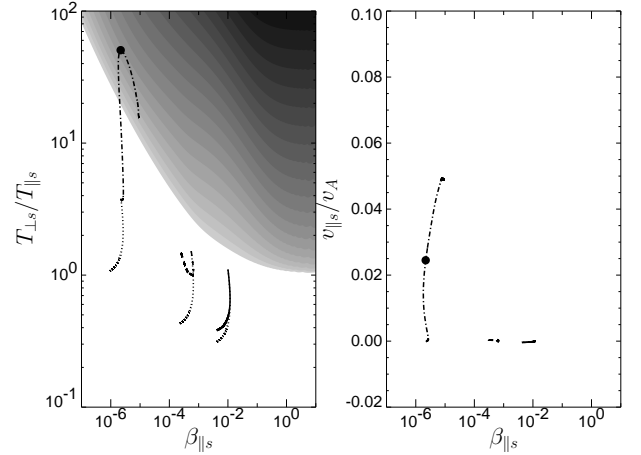


Figure 7. Evolution in run 2: (left) The system path in the space $(\beta_{\parallel s}, T_{\perp s}/T_{\parallel s})$ for the three species: (solid) protons, (dashed) alpha particles, and (dash-dotted) O^{5+} . The dotted curves denote the corresponding predictions of CGL theory and the gray-scale plot denotes the region unstable with respect to the O^{5+} cyclotron instability (in bi-Maxwellian plasma). (right) The system path in the space $(\beta_{\parallel s}, v_{\parallel s}/v_A)$ for three species: (solid) protons, (dashed) alpha particles, and (dash-dotted) O^{5+} . Solid circles denote the oxygen maximum temperature anisotropy point.

The evolution of wave energy in run 2 is shown in Figure 8 (in the same format as in Figure 4). The left panel of Figure 8 shows the fluctuating magnetic field δB multiplied by the factor $(1 + t/t_{\perp})^{3/2}(1 + t/t_{\parallel})^{3/4}$ as a function of time t and the initial wave vector k_0 . The overplotted curves show the approximate cyclotron resonance condition $kv_A = \omega_{cs}$ for (solid) protons, (dashed) alpha particles, and (dash-dotted) O^{5+} .

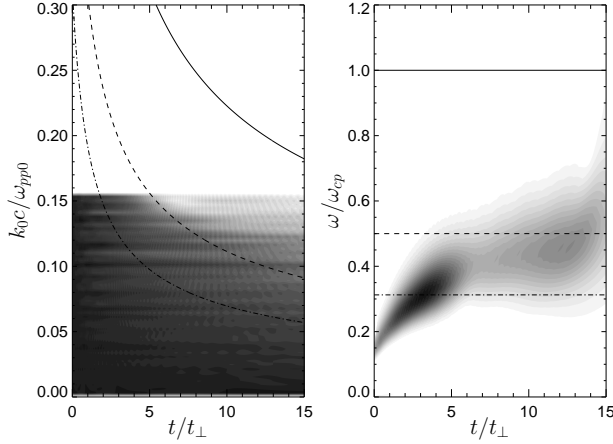


Figure 8. Time evolution in run 2: (left) Gray scale plot of the fluctuating magnetic field δB multiplied by the factor $(1+t/t_{\perp})^{3/2}(1+t/t_{\parallel})^{3/4}$ as a function of time t and the initial wave vector k_0 . The overplotted curves show the approximate cyclotron resonance condition $k v_A = \omega_{cs}$ for (solid) protons, (dashed) alpha particles, and (dash-dotted) O^{5+} . (right) Gray scale plot of the fluctuating magnetic field $\delta B_{k_{\max}}$ multiplied by the factor $(1+t/t_{\perp})^{3/2}(1+t/t_{\parallel})^{3/4}$ as a function of t and ω/ω_{cp} . The overplotted lines show ω_{cs}/ω_{cp} for (solid) protons, (dashed) alpha particles, and (dash-dotted) O^{5+} .

The right panel of Figure 8 shows the fluctuating magnetic field $\delta B_{k_{\max}}$ for the wave vector k_{\max} as a gray scale plot as a function of time t and frequency ω (normalized to ω_{cp}). The spectrum was calculated using the wavelet (Morlet) transform of the time series of $\delta B_{k_{\max}}$. The overplotted lines show the cyclotron frequency ω_{cs}/ω_{cp} for (solid) protons, (dashed) alpha particles, and (dash-dotted) O^{5+} .

Figure 8 (left panel) shows that the wave amplitude δB_k for the different wave vectors k indeed follows the WKB prediction of equation (11)

$$\delta B \left(1 + \frac{t}{t_{\perp}}\right)^{3/2} \left(1 + \frac{t}{t_{\parallel}}\right)^{3/4} \sim \text{const} \quad (19)$$

when far from the cyclotron resonance with the ions. The level of fluctuation only slightly changes when passing through the oxygen resonance whereas the passage through the resonance with the alpha particles damps significantly the wave amplitude. Figure 8, right panel confirms this result: the evolution of the frequency for $\delta B_{k_{\max}}$ shows no significant change near the cyclotron frequency of O^{5+} . Figure 8 indicates that the amount of energy absorbed by oxygen is small with respect to the available wave energy. In the simulation the frequency spectrum smoothly crosses $\omega = \omega_{cO}$, see Figure 8, left panel. These results are essentially the same as observed in the previous section (see Figure 4).

The distribution function of O^{5+} at the maximum temperature anisotropy is far from bi-Maxwellian as documented in Figure 9 which shows the reduced oxygen distribution function $\tilde{f}_O = \tilde{f}_O(v_{\parallel}, v_{\perp})$ (left) at the maximum temperature anisotropy (see Figures 6 and 7, solid circles) and (right) at the end of the simulation. As in Figure 5, $\tilde{f}(v_{\parallel}, v_{\perp})$ is singular around $v_{\perp} \sim 0$. At maximum anisotropy, the electromagnetic ion cyclotron anisotropy instability has not had time to develop, so the primary change here is the increase in perpendicular energy of these heavy ions. This increase, with its characteristic crescent shape, is consistent with pitch-angle scattering by the imposed spectrum of left-handed Alfvén-cyclotron fluctuations. The crescent shape of the distribution function is conserved till the end of the simulation (Figure 9,

right panel). A comparison between the two panels of Figure 9 indicate some diffusion, presumably due to the instability.

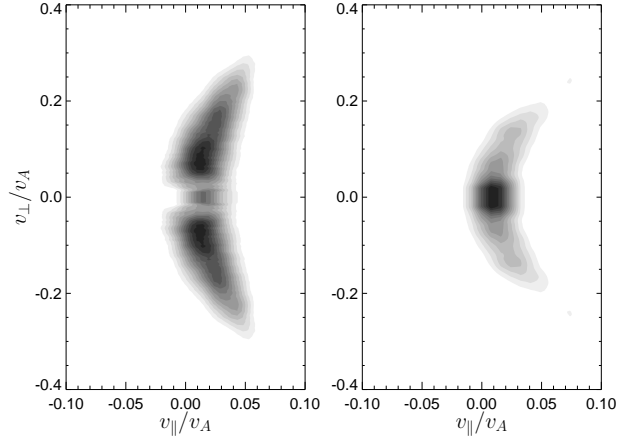


Figure 9. Gray scale plot of the reduced oxygen distribution function $\tilde{f}_O = \tilde{f}_O(v_{\parallel}, v_{\perp})$ (left) at the maximum temperature anisotropy (see Figures 6 and 7, solid circles) and (right) at the end of the simulation.

Returning now to Figure 5, we interpret the distribution at maximum oxygen ion anisotropy as reflecting pitch-angle scattering both by the imposed spectrum and by the electromagnetic oxygen ion anisotropy instability. The former corresponds, as in Figure 9, to the relatively large perpendicular energy ions, whereas the latter is the more dense, relatively isotropic center of the late-time distribution. The instability propagates both parallel and anti-parallel to the background magnetic field, so the consequences of its scattering are to increase the spread in the parallel velocities of the oxygen ions, yielding the relatively isotropic, relatively dense center of the late-time distribution in the right-hand panel of Figure-5.

We performed run 2b without O^{5+} but with the other parameters identical to those of run 2 (see Table 1). Run 2b gives essentially the same results for alpha particles and protons as in run 2. The maximum relative difference between the fluctuating magnetic energies in runs 2 and 2b is about 6 %; this difference is mainly the amount of energy absorbed by the oxygen O^{5+} . In the case of radial expansion the absorption of wave energy by the oxygen O^{5+} seems to be more efficient. But, as in the case of runs 1 and 1b, the presence of O^{5+} does not influence the alpha particles and protons.

3.3. Saturation mechanism

The simulations described in the two previous subsections indicate that oxygen ion saturation of the frequency sweeping mechanism (regardless of the type of the expansion) occurs due to the marginal stabilization of the oxygen cyclotron anisotropy instability. In this subsection we investigate this saturation for a set of simulations with different initial oxygen betas and radial expansion times t_{\parallel} , see Table 1. The dynamics of wave-particle interaction in these additional simulations is qualitatively similar to that in the simulations presented in the previous two sections: we therefore concentrate on the saturation of the frequency sweeping mechanism. Figure 10 summarizes our results for our runs with oxygen (see Table 1): the left panel displays the points at which the heating mechanism saturates in the space $(\beta_{\parallel O}, T_{\perp O}/T_{\parallel O})$, together with the regions unstable to the oxygen cyclotron instability. We assume the saturation to coincide with the maximum oxygen effective temperature anisotropy (see Figures 3 and 7, solid circles). The gray scale denotes the growth rate of the oxygen cyclotron instability in the corresponding bi-Maxwellian plasma. The right panel of Figure 10 shows the same saturation in the space $(\beta_{\parallel O}, v_{\parallel O}/v_A)$.

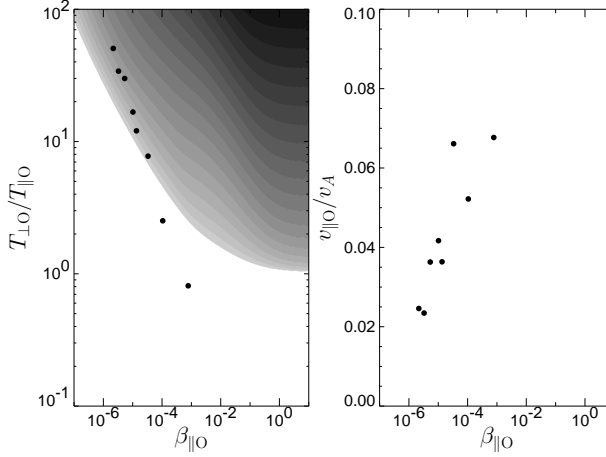


Figure 10. (left) The saturation points for all runs with oxygen (compare with Figures 2, 3, 6, and 7; see also Table 1) in the space $(\beta_{\parallel O}, T_{\perp O}/T_{\parallel O})$. The gray scale denotes the growth rate of the oxygen cyclotron instability in the corresponding bi-Maxwellian plasma. (right) The saturation points in the space $(\beta_{\parallel O}, v_{\parallel O}/v_A)$.

Figure 10 shows that the saturation level of the oxygen temperature anisotropy decreases with $\beta_{\parallel O}$ whereas the saturation oxygen velocity $v_{\parallel O}/v_A$ increases. For about $\beta_{\parallel O} < 4 \cdot 10^{-5}$ the saturation temperature anisotropy lies close to the theoretical (bi-Maxwellian) marginal stability and for higher betas the saturation departs from this relation. The two highest saturation parallel beta cases correspond to the oxygen thermal velocity of the order of 10% of the local Alfvén velocity.

The simulation results indicate that the saturation is dictated by the marginal stability condition of the oxygen cyclotron instability. The actual saturation points are in a good, semi-quantitative agreement with the linear predictions calculated for the bi-Maxwellian distribution function when the oxygen thermal velocity is much smaller than the Alfvén velocity. On the other hand, when the oxygen thermal velocity become comparable with the Alfvén velocity the bi-Maxwellian linear predictions do not apply. In that case the oxygen distribution functions have an important portion of non resonant particles which do not participate in the cyclotron interaction. Moreover, the linear prediction does not include any differential velocity between the ion species whereas in the simulation the oxygen/proton velocity becomes more important when $\beta_{\parallel O}$ increases.

4. Discussion and Conclusion

We have used a 1-D hybrid expanding box code to study the Alfvén-cyclotron mechanism for the heating and acceleration of protons, alpha particles, and a tenuous population of oxygen ions. The model includes in an idealized way both transverse and radial expansion of the solar wind and induces the frequency sweeping effect. Due to the technical limitations of the explicit hybrid code the characteristic expansion times t_{\parallel} and t_{\perp} (see equation (4)) are assumed be of the order 10^3 proton gyroperiods, considerably smaller than the actual solar wind values (see Figure 1). Nevertheless, the ion cyclotron and solar wind expansion scales remain well separated [cf. Galinsky and Shevchenko, 2000] in our simulations, making our results qualitatively, if not quantitatively, applicable to real solar wind situations.

The initial discrete spectrum of Alfvén waves is weak, $\beta_w = 1.25 \times 10^{-3}$, with a power spectrum independent of wavenumber, and with 50 modes in the wave vector range $0.003 \div 0.153c/\omega_{pp0}$. We have chosen a flat power spectrum for the sake of simplicity. While this may not correspond to the power law spectra often observed in situ in the solar wind, it is sufficient for the investigation of wave-particle interactions in the relatively narrow band

of wavenumbers where ion cyclotron damping becomes important. Also it is important to note, that the long box ($L_x = 2048c/\omega_{pp0}$) and many modes used in the simulations guarantee a good overlapping of the cyclotron resonances [Deeskov et al., 1990]; therefore we expect our simulation spectra to yield results similar to those from the continuous, solar wind fluctuation spectra.

The simulations illustrate the dynamics involved in the frequency sweeping mechanism for the heating and acceleration of ions. The plasma-wave system initially follow the CGL and WKB predictions. As the system expands each ion species successively becomes resonant with the waves, first the oxygen ions, then the alpha particles and finally the protons. The heating is efficient for oxygen ions, is much less important for alpha particles, and weak for protons. The simulation results are similar to those reported from quasi-linear models [Cranmer, 2001; Vocks and Marsch, 2002] but indicate a more complex behavior.

In the simulations the oxygen ions do not block wave energy from passing to the alpha cyclotron resonance. This is probably due to the fact that the amount of available energy is much greater than the absorption capacity of oxygen ions and that the heating and acceleration are efficient and fast enough so that the resonance becomes rapidly transparent to the ion cyclotron waves, allowing them to cross over the oxygen cyclotron frequency. A similar transparency is also observed in the model of Vocks and Marsch [2002] where, however, no oxygen dispersion effects are included. The simulations indicate that the saturation mechanism for the scattering of oxygen ions is a marginal stabilization of the system with respect to the oxygen anisotropy instability. This is an equivalent of the marginal stabilization in the quasi-linear models [Cranmer, 2001; Vocks and Marsch, 2002], however, in addition to these models, there are indications that this instability is active in the simulations [cf. Galinsky and Shevchenko, 2000; Isenberg, 2001]: the wave-plasma system follows a marginal stability-like path [see run 2, Figure 7 and cf. Hellinger et al., 2003b; Hellinger and Trávníček, 2005] with respect to this instability. During the scattering oxygen ions are able to absorb only a limited amount of available fluctuating energy. This is in contrast with the results of the quasi-linear models by Cranmer [2001] and Vocks and Marsch [2002] and it may indicate that the minor ion dispersion effects on the dissipation are not negligible.

A small differential oxygen/proton velocity is generated via the Alfvén-cyclotron interaction. This velocity does not seem to be important for saturation, however, the decoupling from the unstable and marginally stable region is probably related to its development. The differential velocity becomes more important as the Alfvén velocity decreases with the expansion [cf. Hollweg, 1999].

The results described here suggest further hybrid code studies are needed to better understand and, where possible, to quantify heavy ion heating by Alfvén-cyclotron fluctuations in the coronal context. Especially it is important to understand the role of the different heavy ion parameters, such as the relative density n_s/n_e , the mass m_s/m_p , the charge q_s/e , and the heavy ion velocity $v_{\parallel s}/v_A$, and the dimensionless magnetic fluctuation energy $|\delta B|^2/B_0^2$ (and the distribution of that energy among various modes). Our simulations have shown that the oxygen ion behavior corresponds to a “test particle” response which does not significantly affect the response of the more dense alphas and protons, and, on the other hand, the alpha particles have an important impact on protons since they are dense enough to block the flow of fluctuation energy toward the proton cyclotron resonance. To answer the question how large must n_s/n_e be (with respect to $|\delta B|^2/B_0^2$ for a given spectrum type) to overcome this test particle response and absorb a significant amount of energy from the fluctuations it is necessary to carry out series of simulations in which n_s/n_e , m_s/m_p , $|\delta B|^2/B_0^2$ and the spectrum properties are varied. Further investigation is also needed to determine the role of $v_{\parallel s}/v_A$ in the range of observed values. In particular, linear theory predicts that heavy ions with $v_{\parallel s}/v_A$ of the order of a few tenths become nonresonant with Alfvén-cyclotron fluctuations. Finally, it is important to investigate the role of the expansion times t_{\perp} and t_{\parallel} and the hypothesis that the ion and expansion scales are well separated.

Appendix: Glossary

Subscripts \perp and \parallel denote the directions with respect to the ambient magnetic field \mathbf{B}_0 as well as the transverse and radial directions, respectively. Subscript s denotes the ion species (p stands for protons, α for alpha particles, and O for oxygen O^{5+} ions) or electrons (e); subscript 0 denotes the initial values. $f_s = f_s(\mathbf{v})$ denotes a distribution function, n_s denotes the number density, and $v_{\parallel s}$ denotes the mean parallel velocity; T_s denotes the (isotropic) temperature whereas $T_{\perp s}$ and $T_{\parallel s}$ denote the perpendicular and parallel temperatures, respectively. n_s , $v_{\parallel s}$, $T_{\perp s}$ and $T_{\parallel s}$ are defined by the discrete equivalents of the following expressions:

$$\begin{aligned} n_s &= \int f_s d^3v \\ v_{\parallel s} &= \frac{1}{n_s} \int v_{\parallel} f_s d^3v \\ T_{\perp s} &= \frac{1}{2n_s} \int v_{\perp}^2 f_s d^3v \\ T_{\parallel s} &= \frac{1}{n_s} \int (v_{\parallel} - v_{\parallel s})^2 f_s d^3v / n_s. \end{aligned} \quad (A1)$$

$\beta_{\parallel s} = n_s k_B T_{\parallel s} / (B_0^2 / 2\mu_0)$ is the parallel beta and the wave beta is given by $\beta_w = \sum_k \delta B_k^2 / B_0^2$. $\omega_{cs} = q_s B / m_s$ and $\omega_{ps} = (n_s e^2 / m_s \epsilon_0)^{1/2}$ denote the cyclotron and plasma frequencies, respectively, $v_{\parallel s}$ and $v_{t\parallel s}$ denote the mean parallel and the thermal velocity of the species s , respectively. In these expressions m_s , q_s , and n_s denote the mass, the charge, and the number density, respectively, B_0 denotes the magnitude of the ambient magnetic field, $B_0 = |\mathbf{B}_0|$, δB_k denotes the magnitude of the fluctuating magnetic field with the wave vector $k = |\mathbf{k}|$; μ_0 and ϵ_0 are the magnetic permeability and the electric permittivity of the vacuum, respectively; ρ is the total ion mass density, $\rho = \sum m_s n_s$, and v_A is the Alfvén velocity defined as $v_A = B_0 / (\mu_0 \rho)^{1/2}$. ω and γ denotes the real frequency and the damping/growth rate, respectively.

The reduced distribution function $\tilde{f}_s = \tilde{f}_s(v_{\parallel}, v_{\perp})$ is given by the discrete equivalent of

$$\tilde{f}_s(v_{\parallel}, v_{\perp}) = \frac{1}{v_{\perp}} \int f_s(v_{\parallel}, v_{\perp}, \varphi) v_{\perp} d\varphi, \quad (A2)$$

where φ is the gyrophase angle. The reduction (the integral/summation in equation (A2)) is an average over the gyrophase φ and includes the v_{\perp} Jacobian term.

Acknowledgments. Authors acknowledge the European Research Training Network ‘‘Theory, Observations and Simulations of Turbulence in Space Plasmas’’, the Czech grant GA AV IAA3042403 and the NASA Solar and Heliospheric Theory program. The Los Alamos portion of this work was carried out under the auspices of the U.S. Department of Energy.

References

Casalbuoni, S., L. D. Zanna, S. R. Habbal, and M. Velli (1999), Coronal plumes and the expansion of pressure-balanced structures in the fast solar wind, *J. Geophys. Res.*, *104*, 9947–9961.

Cranmer, S. R. (2001), Ion cyclotron diffusion of velocity distributions in the extended solar corona, *J. Geophys. Res.*, *106*, 24,937–24,954.

Deeskov, P., K. Elsässer, and F. Jeszczemski (1990), Critical wave spectra for stochastic heating of a magnetized plasma, *Phys. Fluids B*, *2*, 1551–1563.

Galinsky, V. L., and V. I. Shevchenko (2000), Nonlinear cyclotron resonant wave-particle interaction in a nonuniform magnetic field, *Phys. Rev. Lett.*, *85*, 90–93.

Gary, S. P., B. E. Goldstein, and J. T. Steinberg (2001a), Helium ion acceleration and heating by Alfvén/cyclotron fluctuations in the solar wind, *J. Geophys. Res.*, *106*, 24,955–24,964.

Gary, S. P., L. Yin, D. Winske, and L. Ofman (2001b), Electromagnetic heavy ion cyclotron instability: Anisotropy constraint in the solar corona, *J. Geophys. Res.*, *106*, 10,715–10,722.

Gomberoff, L., F. T. Gratton, and G. Gnani (1996), Acceleration and heating of heavy ions by circularly polarized Alfvén waves, *J. Geophys. Res.*, *101*, 15,661–15,666.

Hellinger, P., and P. Trávníček (2005), Magnetosheath compression: Role of characteristic compression time, alpha particle abundances and alpha-proton relative velocity, *J. Geophys. Res.*, *110*, A04210, doi: 10.1029/2004JA010687.

Hellinger, P., P. Trávníček, A. Mangeney, and R. Grappin (2003a), Hybrid simulations of the expanding solar wind: Temperatures and drift velocities, *Geophys. Res. Lett.*, *30*, 1211, doi:10.1029/2002GL016409.

Hellinger, P., P. Trávníček, A. Mangeney, and R. Grappin (2003b), Hybrid simulations of the magnetosheath compression: Marginal stability path, *Geophys. Res. Lett.*, *30*, 1959, doi:10.1029/2003GL017855.

Hollweg, J. V. (1999), Cyclotron resonance in coronal holes: 1. heating and acceleration of protons, O^{5+} , and Mg^{9+} , *J. Geophys. Res.*, *104*, 24,781–24,792.

Hollweg, J. V., and P. A. Isenberg (2002), Generation of the fast solar wind: A review with emphasis on the resonant cyclotron interaction, *J. Geophys. Res.*, *107*, 1147, doi:10.1029/2001JA000270.

Isenberg, P. A. (1984), The ion cyclotron dispersion relation in a proton-alpha solar wind, *J. Geophys. Res.*, *89*, 2133–2141.

Isenberg, P. A. (2001), The kinetic shell model of coronal heating and acceleration by ion cyclotron waves 2. Inward and outward propagating waves, *J. Geophys. Res.*, *106*, 29,249–29,260.

Isenberg, P. A., and M. A. Lee (1996), A dispersive analysis of bispherical pickup ion distributions, *J. Geophys. Res.*, *101*, 11,055–11,066.

Kohl, J. L., et al. (1998), UVCS/SOHO empirical determinations of anisotropic velocity distributions in the solar corona, *Astrophys. J. Lett.*, *501*, L127–L131.

Li, X., S. R. Habbal, J. Kohl, and G. Noci (1998), The effect of temperature anisotropy on observations of Doppler dimming and pumping in the inner corona, *Astrophys. J. Lett.*, *501*, L133–L137.

Liewer, P. C., M. Velli, and B. E. Goldstein (2001), Alfvén wave propagation and ion cyclotron interaction in the expanding solar wind: One-dimensional hybrid simulations, *J. Geophys. Res.*, *106*, 29,261–29,281.

Marsch, E., and C.-Y. Tu (2001), Evidence for pitch angle diffusion of solar wind protons in resonance with cyclotron waves, *J. Geophys. Res.*, *106*, 8357–8362.

Matthews, A. (1994), Current advance method and cyclic leapfrog for 2D multispecies hybrid plasma simulations, *J. Comput. Phys.*, *112*, 102–116.

Ofman, L., A. Viñas, and S. P. Gary (2001), Constraints on the O^{+5} anisotropy in the solar corona, *Astrophys. J. Lett.*, *547*, L175–L178.

Ofman, L., S. P. Gary, and A. Viñas (2002), Resonant heating and acceleration of ions in coronal holes driven by cyclotron resonant spectra, *J. Geophys. Res.*, *107*, 1461, doi:10.1029/2002JA009432.

Torrence, C., and G. P. Compo (1998), A practical guide to wavelet analysis, *Bull. Am. Meteor. Soc.*, *79*, 61–78.

Tu, C.-Y., and E. Marsch (1995), MHD structures, waves and turbulence in the solar wind: Observations and theories, *Space Sci. Rev.*, *73*, 1–210.

Tu, C.-Y., and E. Marsch (2001), On cyclotron wave heating and acceleration of solar wind ions in the outer corona, *J. Geophys. Res.*, *106*, 8233–8252.

Vocks, C., and E. Marsch (2002), Kinetic results for ions in the solar corona with wave-particle interactions and Coulomb collisions, *Astrophys. J.*, *568*, 1030–1042.

Xie, H., L. Ofman, and A. Viñas (2004), Multiple ions resonant heating and acceleration by Alfvén/cyclotron fluctuations in the corona and the solar wind, *J. Geophys. Res.*, *109*, A08103, doi:10.1029/2004JA010501.

P. Hellinger, P. Trávníček Institute of Atmospheric Physics, AS CR, Prague 14131, Czech Republic. (petr.hellinger@ufa.cas.cz; trav@ufa.cas.cz)

M. Velli, University of Florence, Arcetri, Lago E. Fermi, 5, Florence 50125, Italy. (velli@arcetri.astro.it)

S. P. Gary, M.S. D466, Los Alamos National Laboratory, Los Alamos, NM 87545, USA (pgary@lanl.gov)

B. E. Goldstein, P. C. Liewer, JPL, 4800 Oak Grove Drive, MS 159-509 Pasadena, CA, 91109, USA. (bruce.goldstein@jpl.nasa.gov; paullett.liewer@jpl.nasa.gov)